International Journal of Theoretical Physics (2026) 65:46
https://doi.org/10.1007/s10773-026-06263-y

RESEARCH

Flavour Anomalies: A comparative Analysis using a Machine Learning Algorithm

S. Peñaranda[1,2] · **J. Alda**[2,3,4] · **A. Mir**[1,2]

Received: 11 November 2025 / Accepted: 20 January 2026

Abstract

We present an analysis on flavour anomalies in semileptonic rare B-meson decays using an effective field theory approach and assuming that new physics affects only one generation in the interaction basis and non-universal mixing effects are generated by the rotation to the mass basis. A global fit to experimental data is performed, focusing on LFU ratios $R_{D^{(*)}}$ and $R_{J/\psi}$ and branching ratios that exhibit tensions with Standard Model predictions on $B \to K^{(*)}\nu\bar{\nu}$ decays. In our analysis, we use a Machine Learning Montecarlo algorithm, a framework that emulates the highly non-Gaussian structure of the likelihood landscape with minimal training cost. This method enables the generation of high-resolution confidence regions and detailed correlation analyses. By comparing three different scenarios, we show that the one that introduces only mixing between the second and third quark generations and no mixing in the lepton sector, as well as independent coefficients for the singlet and triplet four fermion effective operators, provides the best fit to the experimental data. A comparison with previous results is performed. We highlight the key strengths of the Machine Learning framework in our analysis.

1 Introduction

In the last decade several experimental anomalies related to flavour physics and, in particular, in B-meson decays, have been observed [1–18]. The disagreement between the theoretical predictions in the Standard Model (SM) and the experimental measurements is a clear open

✉ S. Peñaranda
siannah@unizar.es

J. Alda
jorge.alda@pd.infn.it

A. Mir
amir@unizar.es

1 Departamento de Física Teórica, Facultad de Ciencias, Universidad de Zaragoza, Pedro Cerbuna 12, E-50009 Zaragoza, Spain

2 Centro de Astropartículas y Física de Altas Energías (CAPA), Universidad de Zaragoza, Zaragoza, Spain

3 Dipartimento di Fisica ed Astronomia "Galileo Galilei", Università degli Studi di Padova, via F. Marzolo 8, 35131 Padova, Italy

4 Istituto Nazionale di Fisica Nucleare (INFN), Sezione Padova, via F. Marzolo 8, 35131 Padova, Italy

window for searches of physics beyond the SM. A model-independent analysis of the contributions to B-physics observables displaying those discrepancies is highly recommended. The Effective Field Theory (EFT) approach allows us to perform this kind of analysis by focusing on the relevant degrees of freedom and describing the physics one is interested in [19–22]. In this way, we can study the allowed regions of parameter space which are compatible with experimental results.

In order to better identify the possible deviations from the SM behaviour, one can construct ratios of branching ratios, which are "cleaner" observables as hadronic uncertainties largely cancel. For example, the $R_{D^{(*)}}$ ratios,

$$R^{\ell}_{D^{(*)}} = \frac{\mathrm{BR}(B \to D^{(*)}\tau\bar{\nu}_\tau)}{[\mathrm{BR}(B \to D^{(*)}e\bar{\nu}_e) + \mathrm{BR}(B \to D^{(*)}\mu\bar{\nu}_\mu)]/2}\,, \tag{1}$$

whose values in the SM are [23]:

$$R^{SM}_{D} = 0.299 \pm 0.004\,, \qquad R^{SM}_{D^*} = 0.257 \pm 0.005\,. \tag{2}$$

The latest measurements of the $R_{D^{(*)}}$ ratios have been performed at Belle II [16],

$$R^{\ell}_{D^*} = 0.262^{+0.041+0.035}_{-0.039-0.032}\,, \tag{3}$$

and LHCb [17],

$$\begin{aligned} R^{\ell}_{D} &= 0.249 \pm 0.043 \pm 0.047\,, \\ R^{\ell}_{D^*} &= 0.402 \pm 0.081 \pm 0.085\,, \end{aligned} \tag{4}$$

bringing the world average to [24]

$$\begin{aligned} R^{\ell}_{D} &= 0.342 \pm 0.026\,, \\ R^{\ell}_{D^*} &= 0.287 \pm 0.012\,, \end{aligned} \tag{5}$$

which are $1.6\,\sigma$ and $2.5\,\sigma$ above the SM, respectively, with a combined tension of $3.31\,\sigma$.

Another class of B meson observables is $R_{J/\psi}$, defined as the Lepton Flavour Universality (LFU) ratio,

$$R_{J/\psi} = \frac{\mathrm{BR}(B_c \to J/\psi\ \tau\ \nu_\tau)}{\mathrm{BR}(B_c \to J/\psi\ \mu\ \nu_\mu)}\,. \tag{6}$$

At the quark level, it corresponds to a $b \to c\ell\nu$ transition, which is the same transition as the R_D and R_{D^*} ratios. As such, it is natural to examine the $R_{J/\psi}$ ratio looking for a similar anomaly. Indeed, the SM prediction is [25]

$$R^{\mathrm{SM}}_{J/\psi} = 0.258 \pm 0.004\,, \tag{7}$$

while the experimental measurement at LHCb [26]

$$R^{\mathrm{LHCb}}_{J/\psi} = 0.71 \pm 0.17 \pm 0.18\,, \tag{8}$$

displaying a $1.8\,\sigma$ tension. It is interesting to note that the experiments detect an excess of tauonic decays (or equivalently a defect of light lepton decays), which is also the case for the R_D and R_{D^*} anomalies. However, this tension is not present in the recent measurement at CMS [15]

$$R^{\mathrm{CMS}}_{J/\psi} = 0.17^{+0.18+0.21+0.19}_{-0.17-0.22-0.18}\,, \tag{9}$$

which is only $0.3\,\sigma$ away from the SM prediction. The naïve average of both measurements results in [27]

$$R_{J/\psi} = 0.52 \pm 0.20\,, \tag{10}$$

consistent with the SM prediction at the $1.3\,\sigma$ level.

Besides, Belle II has also reported an excess in the $B^+ \to K^+\nu\bar{\nu}$ decay [28], combining inclusive and hadronic tagging,

$$\mathrm{BR}(B^+ \to K^+\nu\bar{\nu}) = (2.3 \pm 0.7) \times 10^{-5}\,, \tag{11}$$

which present a $2.7\,\sigma$ excess as compared to the SM prediction [29],

$$\mathrm{BR}(B^+ \to K^+\nu\bar{\nu})_{\mathrm{SM}} = (0.429 \pm 0.013 \pm 0.02) \times 10^{-5}\,. \tag{12}$$

For the decay into a vector kaon, the 90% confidence level limit set by Belle [30],

$$\mathrm{BR}(B^0 \to K^{*0}\nu\bar{\nu}) < 1.8 \times 10^{-5}\,, \qquad \mathrm{BR}(B^+ \to K^{*+}\nu\bar{\nu}) < 6.1 \times 10^{-5}\,, \tag{13}$$

is at least still a factor of 2 away from the SM prediction [31],

$$\mathrm{BR}(B \to K^*\nu\bar{\nu})_{\mathrm{SM}} = (0.824 \pm 0.099) \times 10^{-5}\,. \tag{14}$$

The experimental data has been used in recent years to constrain New Physics (NP) models. Several global fits have been performed in the literature [19–22, 24, 25, 27, 32–46], and references therein. The present work includes in the global analysis the recent experimental measurements of R_{D^*} [24] and $R_{J/\psi}$ [27], which were not included in [19]. Besides, the latest results for $B^+ \to K^+\nu\bar{\nu}$ decay are also included in the discussion. Crucially, the experimental landscape has undergone a fundamental shift since our previous work: the updated R_K and R_{K^*} measurements from 2022 [47] have resolved the long-standing anomalies in $b \to s\ell^+\ell^-$ transitions, bringing these ratios into agreement with SM predictions. This development, combined with the emergence of a significant excess in $B^+ \to K^+\nu\bar{\nu}$, motivates a complete reconsideration of the operator structure. While the same SMEFT operators that were previously favored remain relevant, their relative importance and the optimal flavor structure have changed dramatically.

In this paper, we demonstrate that this new experimental situation requires allowing independent Wilson coefficients for singlet and triplet operators ($C_1 \neq C_3$), a key distinction from our previous scenarios where we assumed $C_1 = C_3$. This generalization, which we implement in our new Scenario III, provides substantially better fits to the data and reveals a qualitatively different phenomenology. Specifically, it allows us to simultaneously describe the persistent anomalies in $b \to c\tau\nu$ and the new excess in $b \to s\nu\bar{\nu}$ channels while maintaining consistency with the now SM-like $b \to s\,\ell^+\ell^-$ observables.

The paper is organized as follows. Section 2 provides a summary of the relevant terms of the Weak Effective Theory for our analysis, as well as few details on how to perform the statistical fit of the Wilson coefficients involved. We analyse the $b \to c\tau\bar{\nu}$ and the $B \to K^{(*)}\nu\bar{\nu}$ decays, providing the best fit predictions for R_{D^*} and $R_{J/\psi}$ observables and for the $B^+ \to K^+\nu\bar{\nu}$ and $B^0 \to K^{*0}\nu\bar{\nu}$ branching ratios. Section 3 is devoted to the global fits, by including some details of the Machine Learning Montecarlo algorithm used up. At the end of this section we discuss the correlation for the R_{D^*} observable and $B^+ \to K^+\nu\bar{\nu}$ decay. Finally, conclusions are presented in Section 4.

2 Effective Field Theories

The Weak Effective Theory (WET) is formulated at an energy scale below the electroweak scale and the heavy SM states (t, h, $W^\pm$ and Z^0) are integrated out. The NP resides at an energy that is greater than the experimentally accessible energies, and the Wilson coefficients

are a measure of the strength with which the NP couples to ordinary particles. The dimension six operators are constructed from light SM fields. In this section we only present the relevant terms for our analysis from the WET Lagrangian [48–50]. We start by analyzing the $b \to c\tau\bar{\nu}$ decays and then discuss the $B \to K^{(*)}\nu\bar{\nu}$ decays. The best fit predictions for R_{D^*} and $R_{J/\psi}$ observables and for the $B^+ \to K^+\nu\bar{\nu}$ and $B^0 \to K^{*0}\nu\bar{\nu}$ branching ratios are obtained.

2.1 $b \to c\tau\bar{\nu}$ decays

In the WET below the electroweak scale, the expressions for $R_{J/\psi}$ were given by [25, 51], and for $R_{D^{(*)}}$ by [52]. The relevant effective Lagrangian is

$$\mathcal{L}_{b\to c\tau\nu} = -\frac{4G_F}{\sqrt{2}} V_{cb} \left[(1 + C_{VL})\, O_{VL} + C_{VR}\, O_{VR} + C_{SL}\, O_{SL} + C_{SR}\, O_{SR} + C_T\, O_T\right] + \text{h.c.}\,, \tag{15}$$

where G_F is the Fermi constant, V_{cb} is an element of the CKM matrix and the effective operators are defined as

$$\begin{aligned} O_{VL} &= (\bar{c}_L\gamma^\mu b_L)(\bar{\tau}_L\gamma_\mu \nu_L)\,, & O_{VR} &= (\bar{c}_R\gamma^\mu b_R)(\bar{\tau}_L\gamma_\mu \nu_L)\,, \\ O_{SL} &= (\bar{c}_R b_L)(\bar{\tau}_R \nu_L)\,, & O_{SR} &= (\bar{c}_L b_R)(\bar{\tau}_R \nu_L)\,, \\ O_T &= (\bar{c}_R\sigma^{\mu\nu} b_L)(\bar{\tau}_R\sigma_{\mu\nu} \nu_L)\,, \end{aligned} \tag{16}$$

being their corresponding Wilson coefficients C_{VL}, C_{VR}, C_{SL}, C_{SR} and C_T, respectively.

In the SM, the $b \to c\ell\nu$ transitions at tree level are mediated by the exchange of a W boson, which in the WET is integrated out contributing to the $C_{VL}^{\text{tot}} = 1 + C_{VL}$ Wilson coefficient. This contribution has already been separated in Lagrangian (15), and therefore any nonzero value of the Wilson coefficients in the Lagrangian will be due only to NP. The dominant contribution will come from the interference term between C_{VL} and the SM. Furthermore, the scalar contributions C_{SL} and C_{SR} are helicity-suppressed by the mass of the lepton [53].

The NP contributions at an energy scale $\Lambda \sim \mathcal{O}(\text{TeV})$ are defined via the Standard Model Effective Field Theory (SMEFT) Lagrangian [54]. The relevant terms for our analysis can be written as,

$$\mathcal{L}_{\text{SMEFT}} = \frac{1}{\Lambda^2}\left(C^{ijkl}_{\ell q(1)}\, O^{ijkl}_{\ell q(1)} + C^{ijkl}_{\ell q(3)}\, O^{ijkl}_{\ell q(3)}\right)\,, \tag{17}$$

where Λ is the energy scale, ℓ and q are the lepton and quark $SU(2)_L$ doublets, i, j, k, l denote generation indices, and the dimension six operators are defined as

$$O^{ijkl}_{\ell q(1)} = (\bar{\ell}_i\gamma_\mu \ell_j)(\bar{q}_k\gamma^\mu q_l), \qquad O^{ijkl}_{\ell q(3)} = (\bar{\ell}_i\gamma_\mu \tau^I \ell_j)(\bar{q}_k\gamma^\mu \tau^I q_l), \tag{18}$$

with τ^I being the Pauli matrices and $C^{ijkl}_{\ell q(1)}$ and $C^{ijkl}_{\ell q(3)}$ are the corresponding Wilson coefficients. Here we only include the SMEFT operators containing two left-handed quarks and two left-handed leptons motivated by our interest in the B anomalies.

The tree-level matching between the WET and SMEFT coefficients at the scale $\mu = M_Z$ is given by [55]:

$$\begin{aligned} C_{VL} &= -\frac{\sqrt{2}}{4G_F\Lambda^2 V_{cb}}\left(2C^{3323}_{\ell q(3)} - 2C^{23}_{\varphi q(3)}\right)\,, & C_{VR} &= \frac{\sqrt{2}}{4G_F\Lambda^2 V_{cb}} C^{23}_{\varphi ud} \\ C_{SL} &= -\frac{\sqrt{2}}{4G_F\Lambda^2 V_{cb}} C^{3332\,*}_{\ell equ(1)}\,, & C_{SR} &= -\frac{\sqrt{2}}{4G_F\Lambda^2 V_{cb}} C^{3332\,*}_{ledq}\,, \\ C_T &= -\frac{\sqrt{2}}{4G_F\Lambda^2 V_{cb}} C^{3332\,*}_{\ell equ(3)}\,. \end{aligned} \tag{19}$$

It is important to note that the contributions from scalar-quark operators $C_{\varphi q(3)}$ and $C_{\varphi ud}$ are universal in the lepton flavour, and therefore can not contribute to the B-meson anomalies. The contributions from $C_{\ell equ(1)}$, $C_{\ell equ(3)}$ and $C_{\ell edq}$ involve right-handed fermions, which are suppressed because they do not interfere with the SM electroweak interactions.

In order to better understand the impact of NP on $R_{J/\psi}$ and its relation to R_{D^*}, we perform a statistical fit of the three Wilson coefficients C_{VR}, C_{VL} and C_T including both observables. As mentioned before, the contribution of the scalar coefficients are negligible. The fit is performed by numerical minimization of the statistic test χ^2 given by

$$\chi^2_{\text{fit}} = \frac{1}{2}\sum_{i,j}[\mathcal{O}_i^{\text{exp}} - \mathcal{O}_i^{\text{th}}(\{C\})]\,\mathcal{C}_{ij}^{-1}\,[\mathcal{O}_j^{\text{exp}} - \mathcal{O}_j^{\text{th}}(\{C\})]\,, \tag{20}$$

where $\mathcal{O}_i^{\text{exp}}$ and $\mathcal{O}_i^{\text{th}}(\{C\})$ are the experimental measurement and theoretical prediction for the i-th observable, respectively, and $\mathcal{C}_{ij}$ is the correlation matrix. The result of the fit is represented in Fig. 1, by choosing two-dimensional contours of the Wilson coefficients with the rest of the parameters as fixed in the best fit point. The scalar contributions C_{SL} and C_{SR} are suppressed and the fit is constrained by the vector Wilson coefficients C_{VL} and C_{VR} and the tensor coefficient C_T. The values obtained for each coefficient are:

$$C_{VL} = 0.296 \pm 0.167\,, \qquad C_{VR} = -0.409 \pm 0.089\,, \qquad C_T = 0.341 \pm 0.386\,. \tag{21}$$

The predictions for R_D, R_{D^*} and $R_{J/\psi}$ observables and their uncertainties in the best fit point are

$$R_D = 0.342^{+0.039}_{-0.039}\,, \qquad R_{D^*} = 0.288^{+0.022}_{-0.022}\,, \qquad R_{J/\psi} = 0.345^{+0.026}_{-0.029}\,, \tag{22}$$

compatible with the experimental results within $1\,\sigma$.

2.2 $B \to K^{(*)}\nu\bar{\nu}$ decays

In the WET, the $B \to K^{(*)}\nu\bar{\nu}$ processes receive contributions from the effective operators appearing in the Lagrangian [29]

$$\mathcal{L}_{b\to s\nu\bar{\nu}} = -\frac{4G_F}{\sqrt{2}}\frac{\alpha_{\text{em}}}{4\pi}\sum_{\nu,\nu'}\left[(C_L^{\text{NP}\,\nu\nu'} + C_L^{\text{SM}\,\nu\nu'})\,O_L^{\nu\nu'} + C_R^{\nu\nu'}\,O_R^{\nu\nu'}\right] + \text{h.c.}\,, \tag{23}$$

where the semileptonic four-fermion operators are

$$O_L^{\nu\nu'} = (\bar{s}\gamma_\mu P_L b)(\bar{\nu}\gamma^\mu P_L \nu')\,, \qquad O_R^{\nu\nu'} = (\bar{s}\gamma_\mu P_R b)(\bar{\nu}\gamma^\mu P_L \nu')\,, \tag{24}$$

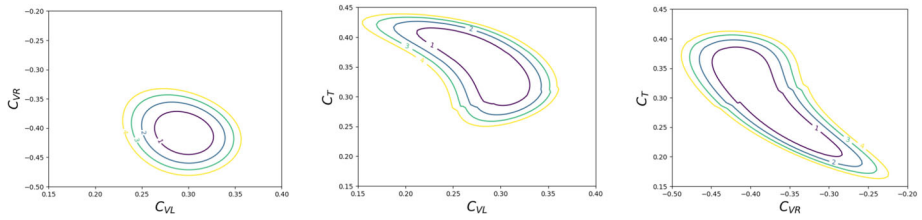

Fig. 1 Fit to the WET parameters to the R_{D^*} and $R_{J/\psi}$ ratios at $1\,\sigma$ (purple), $2\,\sigma$ (blue), $3\,\sigma$ (green) and $4\,\sigma$ (yellow)

being $P_{R,L} = (1 \pm \gamma_5)/2$. The SM matching is $C_L^{\mathrm{SM}\,\nu\nu'} = V_{tb} V_{ts}^* X_{\mathrm{SM}}\, \delta_{\nu\nu'}$, where V_{ij} are the elements of the CKM matrix, and $X_{\mathrm{SM}} = -12.64 \pm 0.15$ [29, 56]. The branching ratios in the WET are calculated as

$$\mathrm{BR}(B^+ \to K^+ \nu\bar{\nu}) = A_+^{BK} \sum_{\nu,\nu'} |(C_L^{\mathrm{NP}\,\nu\nu'} + C_L^{\mathrm{SM}\,\nu\nu'}) + C_R^{\nu\nu'}|^2, \tag{25}$$

$$\begin{aligned}\mathrm{BR}(B^0 \to K^{*0} \nu\bar{\nu}) = {} & A_+^{BK^*} \sum_{\nu,\nu'} |(C_L^{\mathrm{NP}\,\nu\nu'} + C_L^{\mathrm{SM}\,\nu\nu'}) + C_R^{\nu\nu'}|^2 \\ & + A_-^{BK^*} \sum_{\nu,\nu'} |(C_L^{\mathrm{NP}\nu\nu'} + C_L^{\mathrm{SM}\nu\nu'}) - C_R^{\nu\nu'}|^2,\end{aligned} \tag{26}$$

where $A_+^{BK} = (5.66 \pm 0.17) \times 10^{-6}$ [29] and $A_-^{BK^*} = (8.88 \pm 1.08) \times 10^{-6}$, $A_+^{BK^*} = (2.00 \pm 0.29) \times 10^{-6}$ [31].

The tree-level match between the relevant SMEFT and the WET Wilson coefficients is [55]

$$\begin{aligned} C_L^{\mathrm{NP}\,\nu\nu'} &= -\frac{\sqrt{2}\pi}{G_F \Lambda^2 \alpha_{\mathrm{em}}} \left(C_{\ell q(1)}^{\nu\nu' 23} - C_{\ell q(3)}^{\nu\nu' 23} + \delta_{\nu\nu'} C_{\varphi q(1)}^{23} + \delta_{\nu\nu'} C_{\varphi q(3)}^{23} \right), \\ C_R^{\nu\nu'} &= -\frac{\sqrt{2}\pi}{G_F \Lambda^2 \alpha_{\mathrm{em}}} \left(C_{\ell d}^{\nu\nu' 23} + \delta_{\nu\nu'} C_{\varphi d}^{23} \right). \end{aligned} \tag{27}$$

When performing a fit that considers only the parameters C_L^{33} and C_R^{33} (third generation of neutrinos), we observe that the resulting values are located at the intersection between two parallel bands, which occur at $C_L^{33} + C_R^{33} = \text{constant}$, consequence of the constraints

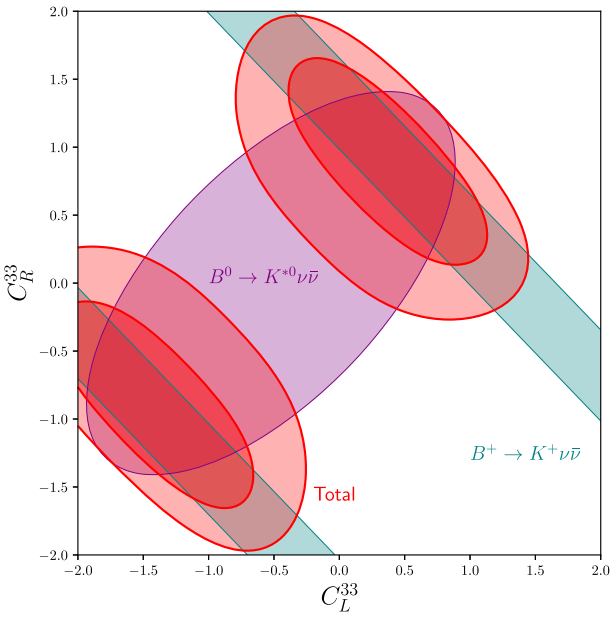

Fig. 2 Fit to the WET parameters for $B \to K^{(*)} \nu\bar{\nu}$ branching ratios. The teal areas correspond to $\mathrm{BR}(B^+ \to K^+ \nu\bar{\nu}) = (2.3 \pm 0.7) \times 10^{-5}$ and the purple area to $\mathrm{BR}(B^0 \to K^{*0} \nu\bar{\nu}) < 1.8 \times 10^{-5}$, while the red areas are the best fit at $1\,\sigma$ and $2\,\sigma$

imposed by the observable $B^+ \to K^+ \nu\bar{\nu}$; and the ellipse that corresponds to the constraints imposed by the observable $B^0 \to K^{0*} \nu\bar{\nu}$ as shown in Fig. 2. The two minima are located at

$$(C_L^{33},\, C_R^{33}) = (-1.4 \pm 0.6,\, -0.9 \pm 0.6) \qquad \text{and} \qquad (C_L^{33},\, C_R^{33}) = (0.4 \pm 0.6,\, 0.9 \pm 0.6) \tag{28}$$

and in both minima the predictions for the observables are

$$\text{BR}(B^+ \to K^+ \nu\bar{\nu}) = (2.2 \pm 0.7) \times 10^{-5}, \qquad \text{BR}(B^0 \to K^{*0} \nu\bar{\nu}) = (1.3 \pm 0.2) \times 10^{-5}\,, \tag{29}$$

compatible with the experimental measurements. Our results are in agreement with the results of [29] for their cLFC scenario. If only couplings to left-handed quarks are allowed, the best fits are obtained for $C_L^{33} = 0.9 \pm 0.3$ or -2.0 ± 0.3, corresponding to $\text{BR}(B^+ \to K^+ \nu\bar{\nu}) = (1.5 \pm 0.6) \times 10^{-5}$ and $\text{BR}(B^0 \to K^{*0} \nu\bar{\nu}) = (1.8 \pm 1.0) \times 10^{-5}$. Therefore, we can conclude that C_L^{33} alone can reduce the tension to the $1\,\sigma$ level, while the addition of C_R^{33} is necessary to fully describe the experimental data.

3 Global Fits

In this section we will update and extend the results obtained in [19], which used a subset of the SMEFT operators first proposed by [57–59]. The dimension-6 Lagrangian in the "Warsaw-down" basis takes the form [19]

$$\mathcal{L}_{\text{NP}} = \frac{\lambda_{ij}^{\ell} \lambda_{kl}^{q}}{\Lambda^2} [C_1 (\bar{\ell}_i \gamma_\mu \ell_j)(\bar{q}_k \gamma^\mu q_\ell) + C_3 (\bar{\ell}_i \gamma_\mu \tau^I \ell_j)(\bar{q}_k \gamma^\mu \tau^I q_\ell)]\,, \tag{30}$$

where ℓ_i and q_i are the $SU(2)_L$ doublets for the i-th generation of leptons and quarks, respectively, Λ is the energy scale where the UV theory is matched to the SMEFT, C_1 and C_3 are the Wilson coefficients for singlet and triplet interactions, with the identification $C_{\ell q(1)}^{ijkl} = C_1 \lambda_{ij}^{\ell} \lambda_{kl}^{q}$ and $C_{\ell q(3)}^{ijkl} = C_3 \lambda_{ij}^{\ell} \lambda_{kl}^{q}$, being λ^ℓ and λ^q the matrices that determine the flavour structure of the NP interactions. We will fix the value $\Lambda = 1$ TeV, which assumes that the NP effects can be observed in flavour physics experiments. Flavour-changing charged currents can only be mediated by triplet interactions, and therefore C_3 is necessary to describe the $R_{D^{(*)}}$ and $R_{J/\psi}$ anomalies. Flavour-changing neutral currents, on the other hand, are mediated by both C_1 and C_3, in particular the contributions to $b \to s\ell^+\ell^-$ are proportional to $C_1 + C_3$, while $b \to s\nu\bar{\nu}$ receives tree-level contributions from $C_1 - C_3$. Finally, the matrices λ are a reflection of the flavour structure of the UV theory. One simple case, proposed by [57], considered that the UV theory only affected one generation of fermions in a certain interaction basis, which needs to be rotated to the mass basis. In this case, the matrices must be hermitian, idempotent ($\lambda^2 = \lambda$) and $\text{tr}\,\lambda = 1$ and, as explained in [19], can be parameterized by two complex numbers, $\alpha^{\ell,q}$ and $\beta^{\ell,q}$, in the following way:

$$\lambda^{\ell,q} = \frac{1}{1 + |\alpha^{\ell,q}|^2 + |\beta^{\ell,q}|^2} \begin{pmatrix} |\alpha^{\ell,q}|^2 & \alpha^{\ell,q} \bar{\beta}^{\ell,q} & \alpha^{\ell,q} \\ \bar{\alpha}^{\ell,q} \beta^{\ell,q} & |\beta^{\ell,q}|^2 & \beta^{\ell,q} \\ \bar{\alpha}^{\ell,q} & \bar{\beta}^{\ell,q} & 1 \end{pmatrix}. \tag{31}$$

In order to be consistent in our analysis, we must not restrict ourselves to the ratios $R_{D^{(*)}}$ and $R_{J/\psi}$. We have performed the fits including all observables implemented by `smelli` version 2.3.3 [60] (nearly 600 in total, covering Higgs decays, diboson production, semileptonic

charm decays, lepton flavour violation, electroweak precision tests, and various B-physics channels) plus $R_{J/\psi}$[1].

This broad inclusion is methodologically essential for several reasons. First, the Lagrangian (30) directly contributes to many other physical observables, for example the previously mentioned $\mathrm{BR}(B \to K^{(*)}\nu\bar{\nu})$ and even Lepton Flavour violating processes, like $B \to K e^{\pm}\mu^{\mp}$, due to the off-diagonal terms of λ^{ℓ}. This way, while the dominant sensitivity to our parameters (C_1, C_3, β^q) comes from B-physics observables, the full set constrains the flavor mixing encoded in λ^q after rotating to the mass basis, breaks approximate degeneracies in the parameter space, and validates the stability of the preferred region. Second, the running of the Renormalization Group equations causes the mixing of the operators in Lagrangian (30) with other SMEFT operators. For example, the insertion of $O_{\ell q(1)}$ ($O_{\ell q(3)}$) is necessary for the one loop corrections to $O_{\varphi q(1)}$ and $O_{\varphi \ell(1)}$ ($O_{\varphi q(3)}$ and $O_{\varphi \ell(3)}$) operators that are relevant for interactions between Z bosons and fermions. Third, including observables from multiple sectors provides crucial null tests: improvements in $b \to c\tau\nu$ or $b \to s\nu\bar{\nu}$ channels should not reappear as new tensions in light-lepton channels, charm physics, or electroweak precision measurements.

The goodness of each fit is evaluated with its difference of χ^2 with respect to the SM, $\Delta\chi^2_{\mathrm{SM}} = \chi^2_{\mathrm{SM}} - \chi^2_{\mathrm{fit}}$, being χ^2_{fit} as defined in (20). Besides, the package `smelli` computes the differences of the logarithms of the likelihood function as $\Delta \log L = -\frac{1}{2}\Delta\chi^2_{\mathrm{SM}}$ and, in order to compare two fits A and B, we use the pull between them in units of σ, defined as [61]

$$\mathrm{Pull}_{A\to B} = \sqrt{2}\mathrm{Erf}^{-1}[F(\Delta\chi^2_A - \Delta\chi^2_B; n_B - n_A)], \tag{32}$$

where Erf^{-1} is the inverse of the error function, F is the cumulative distribution function of the χ^2 distribution and n is the number of degrees of freedom of each fit.

For comparison with our previous results, the SM input parameters are chosen to be the same as in [19] and we have considered the two scenarios defined in this paper. In addition, motivated by the tension in the new $B^+ \to K^+\nu\bar{\nu}$ measurement at Belle II [28] together with the alleviation of the tension in the $R_{K^{(*)}}$ ratios, we have introduced a new scenario called Scenario III:

- **Scenario I:** Includes only mixing between the second and third generations through β^{ℓ} and β^q, that is, $\alpha^{\ell} = \alpha^q = 0$ and $C_1 = C_3 \equiv C$.
- **Scenario II:** The only assumption is $C_1 = C_3 \equiv C$. Mixing with both first and second generation leptons through α^{ℓ}, β^{ℓ}, α^q and β^q is considered.
- **Scenario III:** C_1 and C_3 are independent parameters, and we do not consider mixing in the lepton sector, that is $\alpha^{\ell} = \beta^{\ell} = 0$.

Scenarios I and II assumed that $C_1 = C_3 \equiv C$ because at that time, the $R_{K^{(*)}}$ observables presented deviations as compared to their SM predictions, while the constraints set by the $B \to K^{(*)}\nu\bar{\nu}$ decays were quite stringent. However, at present the experimental situation has reversed, with the tension in the $R_{K^{(*)}}$ ratios disappearing [47] and a new anomaly appearing in $B^+ \to K^+\nu\bar{\nu}$, pointing towards different NP contributions to C_1 and C_3. Scenario III assumes that C_1 and C_3 are independent parameters. Additionally, since there are no longer discrepancies in muonic observables, we do not consider mixing in the lepton sector ($\alpha^{\ell} = \beta^{\ell} = 0$); we are also discarding mixing to the first quark generation since it played no role in our previous fits. In all three scenarios, only real values for the fit parameters are considered.

The results of the best fits to the rotation parameters and the coefficients C are summarized in Table 1. Scenarios I and II present a similar best fit point, with $C \sim -0.12$, $\beta^q = 0.8$

[1] We implemented the observable $R_{J/\psi}$ using the form factors in [51].

Table 1 Results of the best fits to the rotation parameters and the coefficients C in Scenario I, II and III

	Scenario I	Scenario II	Scenario III
C_1	$-0.11^{+0.03}_{-0.04}$	-0.12 ± 0.03	-0.205 ± 0.015
C_3	$-0.11^{+0.03}_{-0.04}$	-0.12 ± 0.03	$-0.12^{+0.02}_{-0.01}$
α^ℓ	–	0.0 ± 0.07	–
β^ℓ	0.00 ± 0.02	0.000 ± 0.014	–
α^q	–	-0.076	–
β^q	$0.78^{+1.22}_{-0.36}$	$0.85^{+1.05}_{-0.6}$	$0.64^{+1.36}_{-0.24}$
Pull	$5.71\,\sigma$	$5.51\,\sigma$	$6.25\,\sigma$
$\Delta\chi^2_{\rm SM}$	39.8	43.12	46.66
p-value	1.2×10^{-8}	3.5×10^{-8}	4.1×10^{-10}

and the rest of the rotation parameters compatible with zero. The $\Delta\chi^2_{\rm SM}$ is also similar, with $\Delta\chi^2_{\rm SM} = 39.8$ in Scenario I and $\Delta\chi^2_{\rm SM} = 43.1$ in Scenario II, which results in Scenario I having a better pull because there are less degrees of freedom, i.e. it is a simpler hypothesis. As anticipated, Scenario III results in a much better fit as compared to Scenarios I and II, since it requires the minimum number of parameters needed to describe simultaneously the anomalies in $R_{D^{(*)}}$ and $B \to K\nu\bar{\nu}$, with $\Delta\chi^2_{\rm SM} = 46.66$ and a pull of $6.25\,\sigma$.

In Scenario III, since $\alpha^\ell = \beta^\ell = 0$, there is no mixing in the leptonic sector, and the NP only affects the third generation, i.e., $\lambda^\ell_{33} = 1$ and $\lambda^\ell_{ij} = 0$ for all the other entries. Meanwhile, with a fit value of β^q close to one, there is a large mixing between the second and third quark generations, resulting in $\lambda^q_{22} = 0.29$, $\lambda^q_{33} = 0.71$ and $\lambda^q_{23} = \lambda^q_{32} = 0.45$. This mixing structure thus provides large contributions to $b \to s\,\nu_\tau\bar{\nu}_\tau$ and $b \to c\,\tau^-\bar{\nu}_\tau$ transitions while leaving $b \to s\,e^+e^-$ and $b \to s\,\mu^+\mu^-$ unaltered at tree level.

The role of each parameter of the fit in constraining each class of observables is shown in Figs. 3 and 4. The one-dimensional slices of the likelihood function for Scenario III is included in Fig. 3. The global fit (in orange) consists of 593 observables. However, it can be seen that it is largely dominated by the two classes of observables that we have been discussing in the previous sections: $b \to c\ell\nu$ (in blue) and $b \to s\nu\bar{\nu}$ (in purple). In particular, the $b \to s\nu\bar{\nu}$ observables determine the likelihood function in the direction of the parameter C_1, both $b \to c\ell\nu$ and $b \to s\nu\bar{\nu}$ contribute to the likelihood function in the direction of C_3, and $b \to c\ell\nu$ observables present the most important contribution to the likelihood in the direction of β^q. A similar picture emerges in Fig. 4 when the contours of

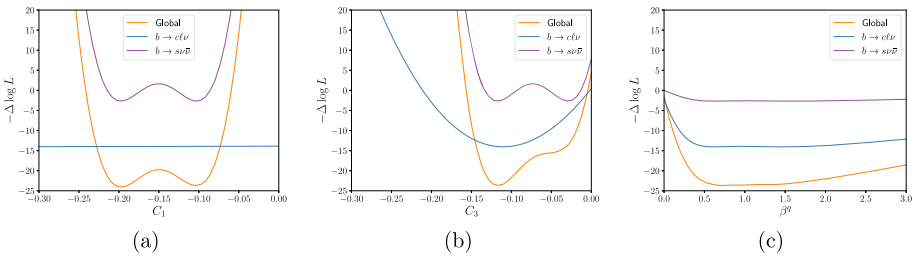

Fig. 3 Negative of the logarithm of the likelihood function when varying (**a**) C_1 (**b**) C_3 and (**c**) β^q with respect to their values at the best fit for Scenario III

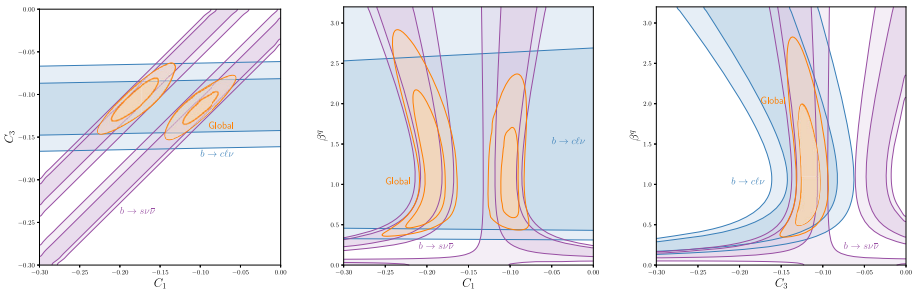

Fig. 4 Regions of constant likelihood in Scenario III for (**a**) C_1 and C_3 plane (**b**) C_1 and β^q plane and (**c**) C_3 and β^q plane, with the rest of parameters as in the best fit point of Scenario III

constant likelihood are considered. As indicated by the matching conditions in (19) and (27), the Wilson coefficient C_{VL} relevant for the $b \to c\ell\nu$ decays depends on $C^{3323}_{\ell q(3)} = C_3 \lambda^q_{23}$ while the coefficient C^{33}_L of the $b \to s\nu\bar{\nu}$ observables depends on both $C^{3323}_{\ell q(1)} = C_1 \lambda^q_{23}$ and $C^{3323}_{\ell q(3)} = C_3\, \lambda^q_{23}$.

After applying the running of the Renormalization Group equation and the matching conditions (see [19] for details), the Wilson coefficients relevant for the $b \to c\,\tau^-\bar{\nu}_\tau$ and $b \to s\,\nu_\tau\,\bar{\nu}_\tau$ processes at the scale $\mu = m_b$ are

$$C_{VL} = 0.089\,, \qquad C^{33}_L = 0.61\,, \tag{33}$$

while the other coefficients in (19) and (27) do not receive contributions from Scenario III. There is also a contribution to the Wilson coefficient C^ℓ_9 which enters the $b \to s\,\ell^+\ell^-$ decays for $\ell = e,\ \mu$ [19, 62]. Since this contribution is generated radiatively from C^τ_9, it is lepton flavour universal for the light flavours, $C^e_9 = C^\mu_9 = -0.58$, and consequently it does not affect the $R_{K^{(*)}}$ ratios, which remain at their SM values $R_{K^{(*)}} \approx 1$. However, this contribution does enter in the branching ratios of $B \to K^{(*)}\mu^+\mu^-$ and $B_s \to \phi\,\mu^+\mu^-$.

We have obtained the predictions for all the observables included in the fit, as well as the pull in the SM and in Scenario III (NP pull). Figure 5 shows the comparison of the pull of each observable with respect to their experimental value in the SM (orange line) and in the Scenario III (blue line). Here the observables in which the SM and Scenario III differ more than $1\,\sigma$ are highlighted. We observe that the highlighted observables are all related to the B-meson anomalies: $R^\ell_{D^*}$ (observable 4) and R^ℓ_D (observable 92) improve by $3.3\,\sigma$ and $1\,\sigma$ respectively; $\mathrm{BR}(B^+ \to K^+\nu\bar{\nu})$ (observable 9) improves by $1.7\,\sigma$ and $\mathrm{BR}(B^+ \to K^{*+}\nu\bar{\nu})$ (observable 161) by $1\,\sigma$ while $\mathrm{BR}(B^0 \to K^{*0}\nu\bar{\nu})$ (observable 144) gets worse by $1\,\sigma$. And finally, regarding the branching ratios of $b \to s\mu^+\mu^-$ at high q^2, $\mathrm{BR}(B^\pm \to K^\pm\mu^+\mu^-)$ in the $[16-17]\,\mathrm{GeV}^2$ (observable 51) and $[15-22]\,\mathrm{GeV}^2$ (observable 87) bins, as well as $\mathrm{BR}(B^\pm_s \to \phi^\pm\mu^+\mu^-)$ in the $[15-19]\,\mathrm{GeV}^2$ bin (observable 111), improve by around $1\,\sigma$ while $\mathrm{BR}(B^\pm \to K^\pm\mu^+\mu^-)$ in the $[17-18]\,\mathrm{GeV}^2$ bin (observable 211) gets worse also by $1\,\sigma$. As pointed out in Section 2.2, it is not possible to describe $B^+ \to K^+\nu\bar{\nu}$ and $B^0 \to K^{*0}\nu\bar{\nu}$ decays only with left-handed effective operators, consequently resulting in a worse pull for $B^0 \to K^{*0}\nu\bar{\nu}$. As for the $B^+ \to K^+\mu^+\mu^-$ differential branching ratios, both LHCb [1] and CMS [18] find some tension between the $[17-18]\,\mathrm{GeV}^2$ bin, which is measured above the SM prediction, and the rest of the bins in the $q^2 \geq 15\,\mathrm{GeV}^2$, which are below their SM prediction, and our fit reproduces said tension.

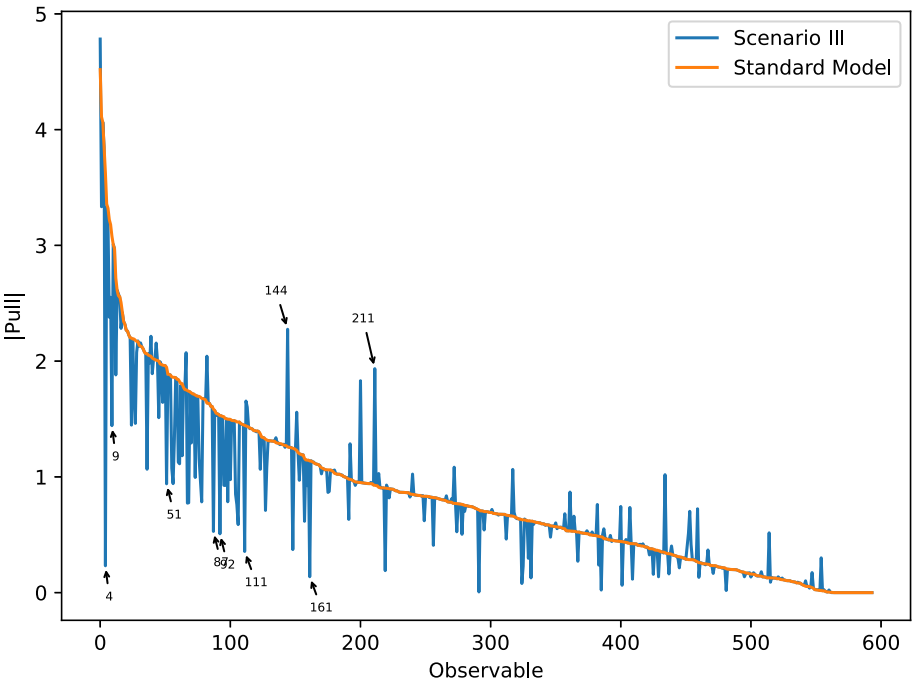

Fig. 5 Pull of the observables considered for the global fit in the SM (orange line) and Scenario III (blue line). The observables are ordered by decreasing SM pull, and the ones in which the SM and Scenario III differ more than $1\,\sigma$ are specially marked

3.1 Comparison with Previous Results

The inclusion of the new experimental measurements at LHCb for $R_{K^{(*)}}$ [47, 63] has significantly impacted our global fit, as compared to previous results presented in [19]. In the previous fit, we found that a sizable contribution to α^ℓ was needed to describe the $R_{K^{(*)}}$ anomaly via NP affecting the electron decay mode. Now that the experimental measurements for $R_{K^{(*)}}$ are compatible with the SM predictions, the current fit no longer requires large deviations in α^ℓ. In consequence, there is no mixing in the leptonic sector, with $\lambda^\ell_{33} \approx 1$ affecting the tau decays (required to describe LFUV in $b \to c\tau\nu_\tau$ processes), while $\lambda^\ell_{ij} \approx 0$ for $ij \neq 33$. In the quark sector, the central values found by the fit present no significant changes as compared to the previous one, with large NP effects in β^q needed to describe the anomalies in flavour-changing $b \to c$ charged currents. However, we observe that β^q presents a larger allowed range, including even regions with $\beta^q > 1$, that is, with larger NP effects in the second generation than in the third generation. In the previous fit, β^q was constrained by the LFV decays $B \to K^{(*)}\mu e$, which received NP contributions through $C\lambda^q_{23}\lambda^\ell_{12} \sim C\beta^q\alpha^\ell\beta^\ell$. With the new fit preferring values of α^ℓ much closer to zero, the impact of β^q in the LFV observables is decreased, and instead, β^q is controlled mainly by the $b \to c\ell\nu$ decays.

This is illustrated in Fig. 6, where the two-dimensional section of the likelihood function for the parameters α^ℓ-β^ℓ in Scenario II, with the rest of the parameters set at the best fit point of this scenario, is compared between the previous fit (left) and the new fit (right). In [19] we found that the better fit, with the inclusion of previous discrepancies on R_K and

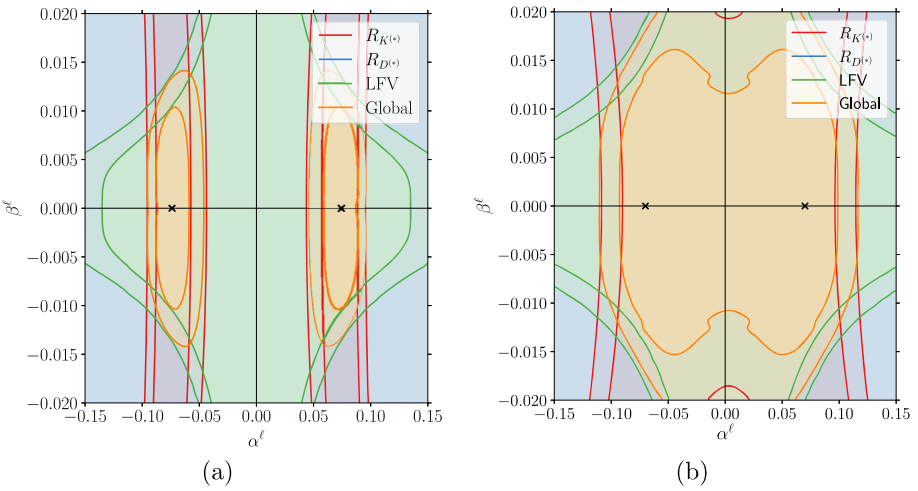

Fig. 6 Regions of constant likelihood for α^ℓ and β^ℓ parameters in Scenario II as (**a**) in the previous work [19] and (**b**) in the current work

R_{K^*} results, corresponded to Scenario II. However, the present experimental measurements of these ratios do not have discrepancies with the SM predictions anymore. In fact, it can be seen that the main difference is the region allowed for the $R_{K^{(*)}}$ observables, inside the red lines: in the previous fit, the allowed region corresponded to $0.04 \leq |\alpha^\ell| \leq 0.10$, which was not compatible with the SM value $\alpha^\ell = 0$ owing to the experimental anomalies at that moment. On the other hand, the allowed region in the current fit is $0 \leq |\alpha^\ell| \leq 0.12$, which includes the SM point since the anomalies are gone. The global fit, in orange, follows the same logic.

The predictions for R_D, R_{D^*} and $R_{J/\psi}$ observables in the best fit points for Scenarios I, II and III are shown in Fig. 7(a). R_D and R_{D^*} exhibit very similar values in both scenarios II and III (as $\alpha^{l,q}$ does not affect these predictions), and these fitted values align well with

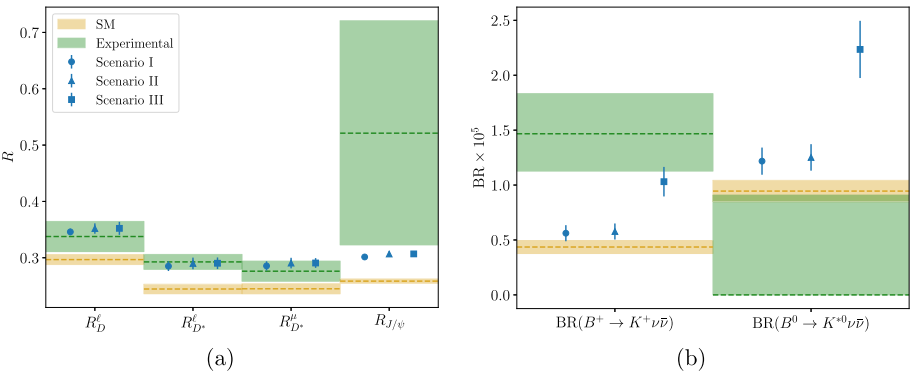

Fig. 7 Predictions for selected (**a**) $b \to c\ell\nu$ LFU ratios and (**b**) $b \to s\nu\bar{\nu}$ branching ratios. The predictions in Scenarios I, II and III and their expected error are represented with blue markers. The SM prediction and its $1\,\sigma$ error are represented by the yellow regions. The experimental measurement and its $1\,\sigma$ error are represented by the green regions

experimental results. The current fit is largely dominated in the $b \to c\ell\nu$ sector by the $R_{D^{(*)}}$ ratios, as their uncertainty is much smaller than in the case of $R_{J/\psi}$. It would be therefore desirable to improve the measurements of $R_{J/\psi}$ in order to obtain an independent handle of the $b \to c\ell\nu$ sector and further clarify the present anomaly.

Figure 7(b) includes the predictions for $B^+ \to K^+\nu\bar{\nu}$ and $B^0 \to K^{*0}\nu\bar{\nu}$ branching ratios, not included in our previous analysis. In both cases we can see how the scenario I and II, in which the coefficients $C_1 = C_3$ were not independent, fail to correctly capture the NP contribution, yielding values very close to the SM predictions. In contrast, Scenario III manages to improve the results in the charged sector, although the results in the neutral sector are worsened.

For comparison, the values obtained for $b \to s\,\ell^+\ell^-$, $b \to c\,\ell\,\nu$ and $b \to s\,\nu\,\bar{\nu}$ observables in Scenario II are presented in Table 2. For each observable, the significance of the deviations with respect to the experimental values, in units of σ, is provided. The ones in the column "Previous fit" are referred to the experimental measurements that were available in Ref. [19], while the ones in the column "Current fit" correspond to the updated values derived in this work. In the case of the $R_{K^{(*)}}$ ratios, the current fit improves the pull for $R_{K^{*0}}^{[1.1,6.0]}$ and $R_{K^{*0}}^{[0.045,1.1]}$, the later by almost $2\,\sigma$. At the same time, the pull for $R_{K^+}^{[1.1,\ 6.0]}$ has increased to $1.1\,\sigma$. The reason for this change is that this is the only bin where some of the tension with the SM prediction still survives, and our fit reproduces this tension. The updated measurements of $R_{D^{(*)}}$ and the inclusion of the observable $R_{J/\psi}$, with its large uncertainty, have a lesser impact on our fit. However, for the $R_{D^{(*)}}$ ratio that includes the decay mode to electrons, $R_{D^*}^{\ell}$, the current fit represents an improvement over the previous one due to the reduced NP effects in α^{ℓ}.

The impact of the new measurement and the reduced NP effects in α^{ℓ} can also be noticed in other $b \to s\,e^+e^-$ observables, for example in the inclusive branching ratio $\mathrm{BR}(B \to X_s\,e^+e^-)$, that has changed from $1.3\,\sigma$ to $1.6\,\sigma$ in the $[14.2,\ 25.0]\,\mathrm{GeV}^2$ bin and from $0.23\,\sigma$ to $0.74\,\sigma$ in the $[1.0,\ 6.0]\,\mathrm{GeV}^2$ bin. Also in LFU ratios, like other bins of $R_{K^{(*)}}$ that were measured by Belle [64], for example $R_{K^0}^{[4.0,\ 8.12]}$ changing from $0.86\,\sigma$ to $1.3\,\sigma$ and $R_{K^+}^{[4.0,\ 8.12]}$ from $1\,\sigma$ to $0.59\,\sigma$. By contrast, $b \to s\,\mu^+\mu^-$ observables like the angular observables

Table 2 Comparison of the predictions for $b \to s\ell^+\ell^-$, $b \to c\ell\nu$ and $b \to s\nu\bar{\nu}$ observables between our previous fit and the current fit in Scenario III

Observable	Previous fit	Current fit
$R_K^{[1.1,\ 6.0]}$	0.83438 ($0.28\,\sigma$)	1.0009 ($1.1\,\sigma$)
$R_{K^{*0}}^{[0.045,1.1]}$	0.88373 ($2.1\,\sigma$)	0.92444 ($0.026\,\sigma$)
$R_{K^{*0}}^{[1.1,6.0]}$	0.84052 ($1.4\,\sigma$)	0.99609 ($0.41\,\sigma$)
R_D^{ℓ}	0.35166 ($0.17\,\sigma$)	0.35131 ($0.51\,\sigma$)
$R_{D^*}^{\ell}$	0.2898 ($0.41\,\sigma$)	0.28951($0.23\,\sigma$)
$R_{D^*}^{\mu}$	0.29041 ($0.75\,\sigma$)	0.28997 ($0.77\,\sigma$)
$R_{J/\psi}$	-	0.30608 ($1.1\,\sigma$)
$\mathrm{BR}(B^+ \to K^+\nu\bar{\nu})$	5.7715×10^{-6} ($1.1\,\sigma$)	9.7026×10^{-6} ($1.4\,\sigma$)
$\mathrm{BR}(B^0 \to K^{*0}\nu\bar{\nu})$	1.2523×10^{-5} ($1.5\,\sigma$)	2.1038×10^{-5} ($2.3\,\sigma$)

The significance of the predictions in the column "Previous fit" are referred to the experimental measurements that were available in Ref. [19], while the significances in the column "Current fit" correspond to the present values

P'_4 and P'_5 or the branching ratios $\mathrm{BR}(B \to K^* \mu^+ \mu^-)$ and $\mathrm{BR}(B_s \to \phi\, \mu^+ \mu^-)$ remain unchanged between both fits, because the value for β^ℓ has not changed.

3.2 Machine Learning Analysis

In this section we detail the Machine Learning (ML) methodology employed in this work, building on the framework established in [19]. While our scenarios contain between 3 and 6 fit parameters (a modest dimensionality for which standard sampling techniques are in principle adequate), we employ an ML-based approach for several compelling reasons that prove essential for this analysis. The confidence intervals extracted from our global fit exhibit pronounced non-Gaussian features: the likelihood surfaces develop curved ridges in the (C_1, C_3, β^q) parameter space, weakly constrained directions emerge from approximate degeneracies, and the mixing of parameters across different scales ($C_1 \sim \mathcal{O}(0.1)$ vs. $\beta^q \sim \mathcal{O}(1)$) complicates straightforward grid-based sampling. These features arise naturally from the interplay between multiple observables with different sensitivities to the Wilson coefficients, and accurately capturing them is crucial for reliable uncertainty propagation to physical predictions.

Given the relatively modest dimensionality of the parameter space, one might expect standard sampling techniques like Markov Chain Monte Carlo (MCMC) to be sufficient. However, the ML emulator offers distinct advantages for this specific analysis due to the likelihood's complex topology. While MCMC is efficient for posterior integration, standard algorithms can struggle to mix efficiently in parameter spaces featuring the narrow, curved ridges present in our global fit. The tree-based regressor adaptively partitions these non-Gaussian boundaries. Furthermore, once trained, the emulator allows for the instantaneous generation of millions of sample points. This computational speed is crucial for producing high-resolution confidence contours and performing the SHAP sensitivity analysis, tasks that would be computationally prohibitive if dependent on running fresh, high-statistics MCMC chains for each projection.

ML, specifically gradient-boosted regression trees implemented via XGBoost (eXtreme Gradient Boosting) algorithm [65], provides an efficient and robust solution tailored to these challenges. The choice of tree-based methods over alternative ML architectures such as neural networks is deliberate and advantageous for our specific use case. Regression trees partition the parameter space in an adaptive manner by sequentially applying binary splits. This approach directs computational resources towards regions of high curvature or rapid variation without assuming global smoothness or continuity. This property is particularly valuable in our context, where the likelihood function exhibits narrow ridges, sharp transitions near best-fit points, and plateau-like regions corresponding to weakly constrained parameter combinations.

Neural networks, by contrast, are universal function approximators that learn smooth interpolations through gradient descent on continuous activation functions. While powerful for high-dimensional problems with abundant training data, they typically require significantly larger training sets and careful regularization to avoid over-smoothing the fine structure present in the likelihood landscape. Moreover, neural networks are prone to over-fitting in low-dimensional regimes without extensive hyperparameter tuning, and their training can be sensitive to initialization and learning rate schedules.

Boosted decision trees, on the other hand, achieve the required accuracy with modest training requirements and provide stable performance under reseeding without extensive tuning. Using the XGBoost algorithm we train an ensemble of regression trees capable of approximating the log-likelihood function of our fit. We build a training sample of 10,500

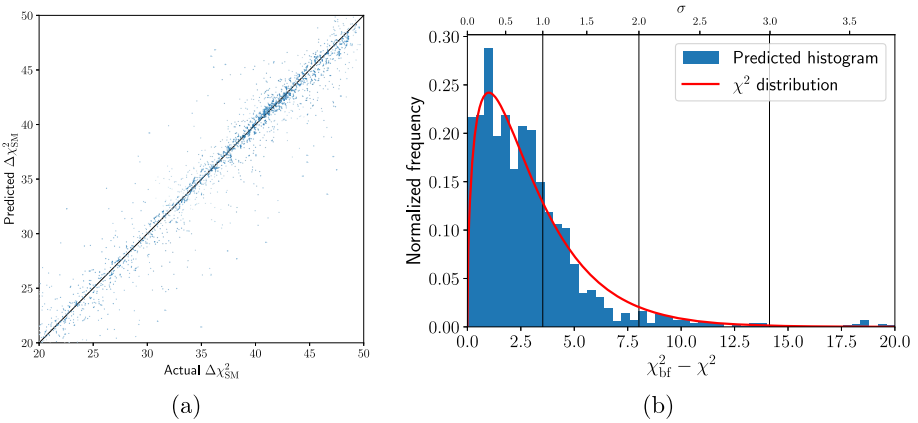

Fig. 8 (**a**) Linear regression between the actual values of the $\Delta\chi^2_{\rm bf}$ (horizontal axis) and the values predicted by the XGBoost model (vertical axis) in the validation set in Scenario III. (**b**) Histogram of the sample of points generated by the ML-based Monte Carlo algorithm in Scenario III, in blue, compared to the χ^2 probability distribution function, in red

parameter points with their corresponding likelihood values and split it into two parts: 84% of the points for training and 16% of the points for validation of the model. We train the ML model with a learning rate of 0.03 and allow early stopping after 5 rounds of stagnant learning. The training process converges after 776 boosting rounds, indicating that the model has learned the essential structure of the likelihood landscape without over-fitting.

The correlation between the actual values of the $\chi^2_{\rm SM}$ in the validation dataset and the corresponding predictions by the ML model is included in Fig. 8(a) for Scenario III. The Pearson coefficient for linear correlation is $r = 0.96$, indicating an excellent agreement. The histogram for the predicted χ^2 values in Fig. 8(b) shows how, once again, the ML-generated points closely follow the general shape of the χ^2 distribution.

Furthermore, tree-based models offer superior interpretability through SHAP (Shapley Additive exPlanations) values, which decompose the model output into additive contributions from each input parameter. SHAP analysis reveals not only the global importance of each parameter but also how individual data points drive the fit quality in different regions of parameter space. This diagnostic is particularly valuable for validating that the dominant constraints indeed arise from the expected B-physics channels, as we demonstrate below. In summary, while neural networks could in principle approximate our likelihood function, the tree-based approach provides the optimal balance of accuracy, efficiency, robustness, and interpretability for the specific characteristics of our $3-6$ dimensional, non-Gaussian fitting problem with moderate training data availability.

We perform a SHAP analysis to quantify the relative contribution of each parameter to the model likelihood. Figure 9 summarizes the global feature importance and directional effects within Scenario III. Features are ordered from top to bottom according to their global importance (mean absolute SHAP value). This hierarchy aligns with the underlying physics: the dominant influence of C_3 reflects the strong sensitivity of the global fit to charged-current observables such as $R_{D^{(*)}}$, while the second largest contribution from C_1 highlights the complementary role of neutral-current processes like $B \to K^{(*)}\nu\bar{\nu}$. The smaller but non-negligible contribution of β^q indicates that quark-mixing effects modulate both sectors without dominating the overall likelihood. This consistency between feature importance and

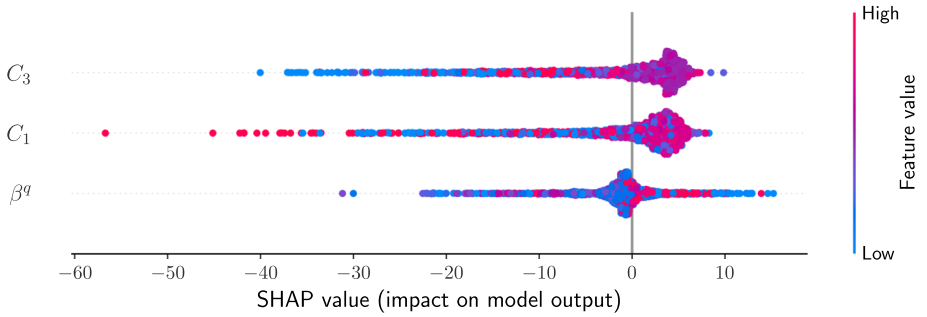

Fig. 9 SHAP summary plot for Scenario III showing the impact of each fit parameter (C_3, C_1, and β^q) on the model output (likelihood). Each point represents a sample from the parameter space, with the horizontal position indicating the SHAP value (contribution to the log-likelihood) and the color indicating the feature value (red for high, blue for low)

the expected physical dominance of charged- and neutral-current operators confirms that the ML approach captures the correct EFT dynamics rather than overfitting numerical noise. The horizontal position of each point represents the SHAP value, corresponding to the impact of that parameter on the log-likelihood, while the color encodes the relative magnitude of the parameter. The plot reveals both the strength and direction of each parameter's influence on the model outcome: broad distributions correspond to features with large overall impact, whereas dense clusters near SHAP ~ 0 mark regions where the model is relatively insensitive to small variations.

We can study the behavior of each feature in detail by plotting the logarithm of the likelihood while varying the other parameters, as shown in Fig. 10. Note that the parameters follow the shapes obtained in the global fit as presented in Fig. 3 (with negative sign). The columns of dots visible in the three plots result from an over-representation of the best-fit points in the data sets for $C_1 = -0.11$, $C_3 = -0.12$ or $\beta^q = 0.6$. This effect arises from using a combination of two different data sets: one with randomly generated points across the parameter space, and another with points in a grid used for the elaboration of Fig. 4. In the latter, each pair of parameters is sampled while keeping the remaining parameter fixed at its best-fit value. We can see this way how increasing or decreasing affects the SHAP values reproducing the behaviour shown in Fig. 9.

We also compare the two-dimensional confidence regions extracted from the ML emulator with those obtained from exact likelihood evaluations. Figure 11 shows the $1\,\sigma$ and $2\,\sigma$ contours in the (C_1, C_3), (C_1, β^q), and (C_3, β^q) planes, with ML-derived contours in blue

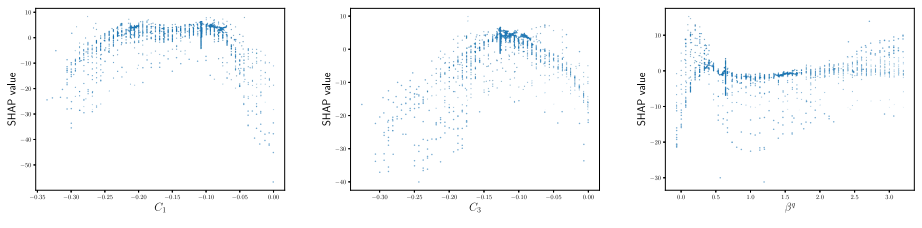

(a) (b) (c)

Fig. 10 Distribution of SHAP values for each parameter of the fit at the sample of 10500 generated points: (**a**) C_1, (**b**) C_3, (**c**) β^q

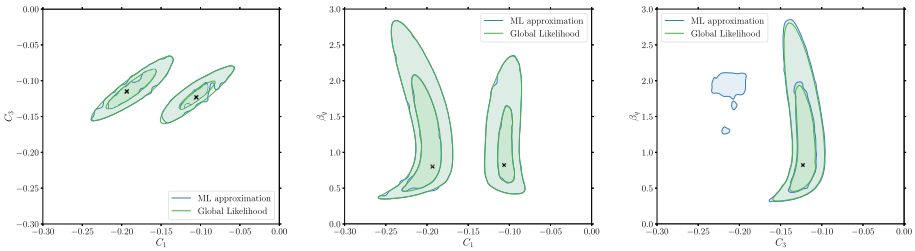

Fig. 11 Comparison between the $1\,\sigma$ and $2\,\sigma$ likelihood contours obtained using the ML approximation (blue) and the actual contours (green) in (**a**) C_1 and C_3 plane, (**b**) C_1 and β^q plane and (**c**) C_3 and β^q plane

and exact contours in green. The excellent agreement across all three projections demonstrates that the emulator accurately captures not only the location of the best-fit point but also the shape, orientation, and extent of the confidence regions. This high-fidelity reconstruction validates the ML approach and enables us to use the rapidly-generated samples for detailed correlation studies and uncertainty propagation that would be computationally prohibitive with exact evaluations alone.

3.2.1 Correlations Between R_{D^*} and BR($B^+ \to K^+ \nu\bar{\nu}$)

The inclusion of the new experimental results on R_{D^*} ratios at Belle II [16], together with the introduction of our new Scenario III, in which the Wilson coefficients C_1 and C_3 are treated as independent parameters and lepton-sector mixing is neglected, leads to substantial modifications of results obtained in [19]. In that study, we found an almost-perfect correlation between these two observables. Figure 12 presents the ML-generated predictions for R_{D^*} and BR($B^+ \to K^+ \nu\bar{\nu}$) in Scenario II (as considered in the previous work) and Scenario III.

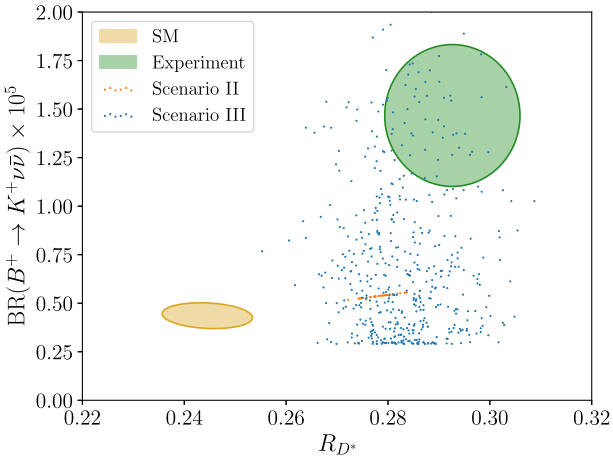

Fig. 12 Values of the observables R_{D^*} and BR($B^+ \to K^+ \nu\bar{\nu}$) in the ML-generated samples for scenario II (orange points) and scenario III (blue points), compared to the SM prediction (yellow region) and experimental measurement (green region)

As can be seen, the strong correlation observed in Scenario II disappears once Scenario III is considered.

The lack of a consistent correlation between the enhanced $B^+ \to K^+ \nu\bar{\nu}$ branching ratios and R_{D^*} raises important questions about lepton flavor universality and the potential presence of NP phenomena. Further experimental results and theoretical works are necessary to clarify these discrepancies and to understand the underlying physics.

Constructing a UV complete model that reproduces the interplay between R_{D^*} and $\mathrm{BR}(B^+ \to K^+ \nu\bar{\nu})$ is out of the scope of this work. Nevertheless, several frameworks proposed in the literature account for the $R_{D^{(*)}}$ anomalies while enhancing $\mathrm{BR}(B^+ \to K^+ \nu\bar{\nu})$. These include models based on vector leptoquarks [66, 67], non-universal Z' bosons [68] or scenarios involving combined scalars and fermions sectors [69]. Our EFT analysis identifies the essential operator structure and flavor patterns that such UV completions must satisfy to remain consistent with the full set of flavor and electroweak constraints.

In summary, this section demonstrates that the ML framework provides essential capabilities for this analysis: accurate emulation of the non-Gaussian likelihood landscape with modest training requirements, efficient generation of large representative samples for high-resolution confidence regions and correlation studies, robust performance without extensive hyperparameter tuning or sensitivity to initialization, and interpretability through SHAP analysis that validates the physical consistency of the fit. These advantages, particularly when compared to alternative methods such as neural networks or brute-force grid sampling, justify the central role of ML in our methodology and demonstrate its value as a quantitative tool for precision phenomenology in particle physics.

4 Conclusions

In this work, we have performed an analysis of the anomalies in B-meson decays by using an effective field theory approach and considering the NP effects on the Wilson coefficients of the effective Lagrangian. The new deviation observed on $B^+ \to K^+ \nu\bar{\nu}$ decay at Belle II is included in the global fits. Consequently, a new scenario (Scenario III) is considered in the present study, with only mixing between the second and third quark generations and no mixing in the lepton sector, being the Wilson coefficients for the singlet and triplet four fermion effective operators independent. Both the recent experimental measurements of $\mathrm{BR}(B^+ \to K^+ \nu\bar{\nu})$ and $R_{J/\psi}$ are included in the analysis. Besides, branching ratios associated with $B \to D^{(*)} \tau \nu$ decays are considered. The fact that the global fit is dominated by these classes of observables underlines their potential as probes to NP.

We use a ML algorithm in our analysis, by checking the agreement between the results obtained for this procedure and both the general shape of the $\Delta\chi^2$ distribution and the analysis of the impact of each parameter on the global fit. In our Scenario III, the $B \to K^{(*)} \nu\bar{\nu}$ observables constrain the parameter C_1, both $B \to D^{(*)} \ell\nu$ and $B \to K^{(*)} \nu\bar{\nu}$ constrain C_3, and $B \to D^{(*)} \ell\nu$ observables present the most important constraint to β^q. The results of the global fit after including a wide range of flavour and electroweak observables are displayed in Table 1, and the predictions for the most relevant observables are summarized in Table 2. The comparison with the previous scenarios considered in [19] is included in the discussion. Our results show that Scenario III, which introduces independent parameters C_1 and C_3 without mixing in the lepton sector, provides the best fit to experimental results, achieving a pull of $6.25\,\sigma$. This scenario successfully accounts for the discrepancies observed in R_{D^*} and $R_{J/\psi}$ measurements while maintaining consistency with the Standard Model in the R_K ratios.

Furthermore, it improves the predicted branching ratio for $\mathrm{BR}(B^+ \to K^+ \nu\bar{\nu})$ although it does not fully explain $\mathrm{BR}(B^0 \to K^{*0} \nu\bar{\nu})$. It is worth noting that this tension in the neutral mode points to a limitation in the assumed flavor structure of Scenario III. Our analysis relies on left-handed SMEFT operators (C_1, C_3) which strictly correlate the charged and neutral channels. Reconciling the current experimental divergence between $B^+ \to K^+ \nu\bar{\nu}$ and $B^0 \to K^{*0} \nu\bar{\nu}$ would likely require the inclusion of right-handed currents or more complex flavor structures beyond the minimal set considered here, as the fit is currently driven by the dominant signals in $R_{D^{(*)}}$ and the charged neutrino mode.

The results are pointing in the direction of NP that interacts mainly with the third generation of leptons, reminiscent of the $U(2)$ flavour symmetry hypothesis [70, 71]. The situation would be clarified further with measurements of $R_{J/\psi}$ achieving a resolution similar to that of $R_{D^{(*)}}$, and with additional τ observables, for example the longitudinal polarisation in $B_c \to J/\psi \tau \nu$ or the branching ratio of $B \to K^{(*)} \tau^+ \tau^-$.

We developed and applied an ML framework that emulates the highly non-Gaussian structure of the likelihood landscape with minimal training cost. Our results show that this method significantly improves accuracy, efficiency, and interpretability. It enables the generation of high-resolution confidence regions and detailed correlation analyses. Additionally, the method remains robust to hyperparameter choices, and offers transparent interpretability through SHAP analysis. Together, these features establish ML as a powerful and reliable tool for global fits in precision particle phenomenology, outperforming conventional approaches such as neural networks and grid sampling.

Acknowledgements This work is partially supported by Spanish MINECO/FEDER Grants No. PGC2022-126078NB-C21 funded by MCIN/AEI/10.13039/ 501100011033 and "ERDF A way of making Europe" and Grant DGA-FSE Grant 2020-E21-17R Aragón Government and the European Union - NextGenerationEU Recovery and Resilience Program on *Astrofísica y Física de Altas Energías* CEFCA-CAPA-ITAINNOVA. Additionally, J.A has received funding from the Fundación Ramón Areces "Beca para ampliación de estudios en el extranjero en el campo de las Ciencias de la Vida y de la Materia".

Author Contributions All authors contributes in writing the main manuscript and prepare the figure, as well as reviewed the manuscript.

Funding Funding information - not applicable.

Data Availability No datasets were generated or analysed during the current study.

Declarations

Competing interests The authors declare no competing interests.

References

1. LHCb Collaboration, Aaij, R., et al.: Differential branching fractions and isospin asymmetries of $B \to K^{(*)}\mu^+\mu^-$ decays. JHEP **06**, 133 (2014). arXiv:1403.8044 [hep-ex]
2. LHCb Collaboration, Aaij, R., et al.: Test of lepton universality using $B^+ \to K^+\ell^+\ell^-$ decays. Phys. Rev. Lett. **113**, 151601 (2014). arXiv:1406.6482 [hep-ex]
3. LHCb Collaboration, Aaij, R., et al.: Angular analysis and differential branching fraction of the decay $B_s^0 \to \phi\mu^+\mu^-$. JHEP **09**, 179 (2015). arXiv:1506.08777 [hep-ex]
4. LHCb Collaboration, Aaij, R., et al.: Angular analysis of the $B^0 \to K^{*0}\mu^+\mu^-$ decay using 3 fb^{-1} of integrated luminosity. JHEP **02**, 104 (2016). arXiv:1512.04442 [hep-ex]
5. LHCb Collaboration, Aaij, R., et al.: Measurements of the S-wave fraction in $B^0 \to K^+\pi^-\mu^+\mu^-$ decays and the $B^0 \to K^*(892)^0\mu^+\mu^-$ differential branching fraction. JHEP **11**, 047 (2016). arXiv:1606.04731 [hep-ex]. [Erratum: JHEP 04, 142 (2017)]
6. CMS, LHCb Collaboration, Khachatryan, V., et al.: Observation of the rare $B_s^0 \to \mu^+\mu^-$ decay from the combined analysis of CMS and LHCb data. Nat. **522**, 68–72 (2015). arXiv:1411.4413 [hep-ex]
7. LHCb Collaboration, Aaij, R., et al.: Measurement of the ratio of branching fractions $\mathcal{B}(\bar{B}^0 \to D^{*+}\tau^-\bar{\nu}_\tau)/\mathcal{B}(\bar{B}^0 \to D^{*+}\mu^-\bar{\nu}_\mu)$. Phys. Rev. Lett. **115**(11):111803 (2015). https://doi.org/10.1103/PhysRevLett.115.111803, arXiv:1506.08614 [hep-ex]. [Erratum: Phys.Rev.Lett. 115, 159901 (2015)]
8. LHCb Collaboration, Aaij, R., et al.: Measurement of the phase difference between short- and long-distance amplitudes in the $B^+ \to K^+\mu^+\mu^-$ decay. Eur. Phys. J. C **77**(3):161 (2017). https://doi.org/10.1140/epjc/s10052-017-4703-2, arXiv:1612.06764 [hep-ex]
9. LHCb Collaboration, Aaij, R., et al.: Measurement of the $B_s^0 \to \mu^+\mu^-$ branching fraction and effective lifetime and search for $B^0 \to \mu^+\mu^-$ decays. Phys. Rev. Lett. **118**(19):191801 (2017). https://doi.org/10.1103/PhysRevLett.118.191801, arXiv:1703.05747 [hep-ex]
10. LHCb Collaboration, Aaij, R., et al.: Search for the decays $B_s^0 \to \tau^+\tau^-$ and $B^0 \to \tau^+\tau^-$. Phys. Rev. Lett. **118**(25), 251802 (2017). https://doi.org/10.1103/PhysRevLett.118.251802, arXiv:1703.02508 [hep-ex]
11. LHCb Collaboration, Aaij, R., et al.: Test of lepton universality with $B^0 \to K^{*0}\ell^+\ell^-$ decays. JHEP **08**, 055 (2017). https://doi.org/10.1007/JHEP08(2017)055, arXiv:1705.05802 [hep-ex]
12. LHCb Collaboration, Aaij, R., et al.: Measurement of the ratio of the $B^0 \to D^{*-}\tau^+\nu_\tau$ and $B^0 \to D^{*-}\mu^+\nu_\mu$ branching fractions using three-prong τ-lepton decays. Phys. Rev. Lett. **120**(17), 171802 (2018). https://doi.org/10.1103/PhysRevLett.120.171802, arXiv:1708.08856 [hep-ex]
13. LHCb Collaboration, Aaij, R., et al.: Evidence for the decay $B_S^0 \to \overline{K}^{*0}\mu^+\mu^-$. JHEP **07**, 020 (2018). https://doi.org/10.1007/JHEP07(2018)020, arXiv:1804.07167 [hep-ex]
14. LHCb Collaboration, Aaij, R., et al.: Search for lepton-universality violation in $B^+ \to K^+\ell^+\ell^-$ decays. Phys. Rev. Lett. **122**, (19): 191801 (2019). https://doi.org/10.1103/PhysRevLett.122.191801, arXiv:1903.09252 [hep-ex]
15. CMS Collaboration, Collaboration, C.: Test of lepton flavor universality violation in semileptonic B_c^+ meson decays at CMS. https://cds.cern.ch/record/2868988
16. Belle-II Collaboration, Adachi, I., et al.: Test of lepton flavor universality with a measurement of R(D*) using hadronic B tagging at the Belle II experiment. Phys. Rev. D **110**, (7), 072020 (2024). https://doi.org/10.1103/PhysRevD.110.072020, arXiv:2401.02840 [hep-ex]
17. LHCb Collaboration, Aaij, R., et al.: Measurement of the branching fraction ratios $R(D^+)$ and $R(D^{*+})$ using muonic τ decays. arXiv:2406.03387 [hep-ex]
18. CMS Collaboration, Hayrapetyan, A., et al.: Test of lepton flavor universality in $B^\pm \to K^\pm\mu^+\mu^-$ and $B^\pm \to K^\pm e^+e^-$ decays in proton-proton collisions at $\sqrt{s}$ = 13 TeV. Rept. Prog. Phys. **87**(7), 077802 (2024). arXiv:2401.07090 [hep-ex]
19. Alda, J., Guasch, J., Penaranda, S.: Using Machine Learning techniques in phenomenological studies on flavour physics. JHEP **07**, 115 (2022). https://doi.org/10.1007/JHEP07(2022)115. arXiv:2109.07405 [hep-ph]
20. Alda, J., Guasch, J., Penaranda, S.: Anomalies in B mesons decays: Present status and future collider prospects. In international workshop on future linear colliders. **5** (2021). arXiv:2105.05095 [hep-ph]
21. Alda, J., Guasch, J., Penaranda, S.: Anomalies in B mesons decays: A phenomenological approach. Eur. Phys. J. Plus **137**(2), 217 (2022). https://doi.org/10.1140/epjp/s13360-022-02405-3. arXiv:2012.14799 [hep-ph]
22. Alda Gallo, J., Guasch, J., Penaranda, S.: Exploring B-physics anomalies at colliders. PoS EPS-HEP2021 **494** (2022). https://doi.org/10.22323/1.398.0494, arXiv:2110.12240 [hep-ph]

23. Jaiswal, S., Nandi, S., Patra, S.K.: Extraction of $|V_{cb}|$ from $B \to D^{(*)}\ell\nu_\ell$ and the Standard Model predictions of $R(D^{(*)})$. JHEP **12**, 060 (2017). https://doi.org/10.1007/JHEP12(2017)060. arXiv:1707.09977 [hep-ph]
24. Heavy flavor averaging group. (2024). https://hflav-eos.web.cern.ch/hflav-eos/semi/moriond24/html/RDsDsstar/RDRDs.html
25. Tang, R.-Y., Huang, Z.-R., Lü, C.-D., Zhu, R.: Scrutinizing new physics in semi-leptonic B $_c \to J/\psi\tau\nu$ decay. J. Phys. G series **49**(11), 115003 (2022). arXiv:2204.04357 [hep-ph]
26. LHCb Collaboration, R. Aaij et al.: Measurement of the ratio of branching fractions $\mathcal{B}(B_c^+ \to J/\psi\tau^+\nu_\tau)/\mathcal{B}(B_c^+ \to J/\psi\mu^+\nu_\mu)$. Phys. Rev. Lett. **120**(12), 121801 (2018). arXiv:1711.05623 [hep-ex]
27. Iguro, S., Kitahara, T., Watanabe, R.: Global fit to b$\to c\tau\nu$ anomalies as of Spring 2024. Phys. Rev. D **110**(7), 075005 (2024). arXiv:2405.06062 [hep-ph]
28. Belle-II Collaboration, I. Adachi et al.: Evidence for B+ $\to K + \nu\nu^-$ decays. Phys. Rev. D **109**(11), 112006 (2024). arXiv:2311.14647 [hep-ex]
29. Bause, R., Gisbert, H., Hiller, G.: Implications of an enhanced B$\to K\nu\nu^-$ branching ratio. Phys. Rev. D **109**(1), 015006 (2024). arXiv:2309.00075 [hep-ph]
30. Belle Collaboration, J. Grygier et al.: Search for $\boldsymbol{B \to h\nu\bar{\nu}}$ decays with semileptonic tagging at Belle. Phys. Rev. D **96**(9), 091101 (2017). arXiv:1702.03224 [hep-ex]. [Addendum: Phys.Rev.D 97, 099902 (2018)]
31. Bause, R., Gisbert, H., Golz, M., Hiller, G.: Interplay of dineutrino modes with semileptonic rare B-decays. JHEP **12**, 061 (2021). arXiv:2109.01675 [hep-ph]
32. Calibbi, L., Crivellin, A., Ota, T.: Effective Field Theory Approach to $b \to s\ell\ell^{(')}$, $B \to K^{(*)}\nu\bar{\nu}$ and $B \to D^{(*)}\tau\nu$ with Third Generation Couplings. Phys. Rev. Lett. **115**, 181801 (2015). arXiv:1506.02661 [hep-ph]
33. Capdevila, B., Crivellin, A., Descotes-Genon, S., Matias, J., Virto, J.: Patterns of New Physics in $b \to s\ell^+\ell^-$ transitions in the light of recent data. JHEP **01**, 093 (2018). arXiv:1704.05340 [hep-ph]
34. Celis, A., Fuentes-Martin, J., Vicente, A., Virto, J.: Gauge-invariant implications of the LHCb measurements on lepton-flavor nonuniversality. Phys. Rev. D **96**(3), 035026 (2017). arXiv:1704.05672 [hep-ph]
35. Alok, A.K., Bhattacharya, B., Datta, A., Kumar, D., Kumar, J., London, D.: New Physics in $b \to s\mu^+\mu^-$ after the Measurement of R_{K^*}. Phys. Rev. D **96**(9), 095009 (2017). arXiv:1704.07397 [hep-ph]
36. Camargo-Molina, J.E., Celis, A., Faroughy, D.A.: Anomalies in Bottom from new physics in Top. Phys. Lett. B **784**, 284–293 (2018). arXiv:1805.04917 [hep-ph]
37. Datta, A., Kumar, J., London, D.: The B anomalies and new physics in $b \to se^+e^-$. Phys. Lett. B **797**, 134858 (2019). arXiv:1903.10086 [hep-ph]
38. Aebischer, J., Altmannshofer, W., Guadagnoli, D., Reboud, M., Stangl, P., Straub, D.M.: B-decay discrepancies after Moriond 2019. Eur. Phys. J. C **80**(3), 252 (2020). arXiv:1903.10434 [hep-ph]
39. Aoude, R., Hurth, T., Renner, S., Shepherd, W.: The impact of flavour data on global fits of the MFV SMEFT. JHEP **12**, 113 (2020). arXiv:2003.05432 [hep-ph]
40. Algueró, M., Matias, J., Capdevila, B., Crivellin, A.: Disentangling lepton flavor universal and lepton flavor universality violating effects in b$\to s\ell + \ell$- transitions. Phys. Rev. D **105**(11), 113007 (2022). arXiv:2205.15212 [hep-ph]
41. N. R. Singh Chundawat, CP violation in $b \to s\ell\ell$: a model independent analysis. Phys. Rev. D **107**, 075014 (2023). arXiv:2207.10613 [hep-ph]
42. Grunwald, C., Hiller, G., Kröninger, K., Nollen, L.: More synergies from beauty, top, Z and Drell-Yan measurements in SMEFT. JHEP **11**, 110 (2023). arXiv:2304.12837 [hep-ph]
43. Bartocci, R., Biekötter, A., Hurth, T.: A global analysis of the SMEFT under the minimal MFV assumption. JHEP **05**, 074 (2024). arXiv:2311.04963 [hep-ph]
44. Elmer, N., Madigan, M., Plehn, T., Schmal, N.: Staying on Top of SMEFT-Likelihood Analyses. arXiv:2312.12502 [hep-ph]
45. Capdevila, B., Crivellin, A., Matias, J.: Review of semileptonic B anomalies. Eur. Phys. J. ST **1**, 20 (2023). arXiv:2309.01311 [hep-ph]
46. Grunwald, C., Hiller, G., Kröninger, K., Nollen, L.: Predicting $B(B \to K^{(*)}\nu\bar{\nu})$ within the MFV-SMEFT using B, Top, Z and Drell-Yan data. PoS EPS-HEP2023 (2024) 298
47. LHCb Collaboration, R. Aaij et al.: Test of lepton universality in $b \to s\ell^+\ell^-$ decays. Phys. Rev. Lett. **131**(5), 051803 (2023). arXiv:2212.09152 [hep-ex]
48. Buras, A. J.: Weak Hamiltonian, CP violation and rare decays. In: Les Houches Summer School in Theoretical Physics, Session 68: Probing the Standard Model of Particle Interactions, pp. 281–539. 6 (1998). arXiv:hep-ph/9806471
49. Aebischer, J., Crivellin, A., Fael, M., Greub, C.: Matching of gauge invariant dimension-six operators for $b \to s$ and $b \to c$ transitions. JHEP **05**, 037 (2016). arXiv:1512.02830 [hep-ph]

50. Aebischer, J., Fael, M., Greub, C., Virto, J.: B physics Beyond the Standard Model at One Loop: Complete Renormalization Group Evolution below the Electroweak Scale. JHEP **09**, 158 (2017). arXiv:1704.06639 [hep-ph]
51. HPQCD Collaboration, Harrison, J., Davies, C. T. H., Lytle, A.: $B_c \to J/\psi$ form factors for the full q^2 range from lattice QCD. Phys. Rev. D **102**(9), 094518 (2020). arXiv:2007.06957 [hep-lat]
52. Tanaka, M., Watanabe, R.: New physics in the weak interaction of $\bar{B} \to D^{(*)}\tau\bar{\nu}$. Phys. Rev. D **87**(3), 034028 (2013). arXiv:1212.1878 [hep-ph]
53. Sakaki, Y., Tanaka, M., Tayduganov, A., Watanabe, R.: Testing leptoquark models in $\bar{B} \to D^{(*)}\tau\bar{\nu}$. Phys. Rev. D **88**(9), 094012 (2013). arXiv:1309.0301 [hep-ph]
54. Grzadkowski, B., Iskrzynski, M., Misiak, M., Rosiek, J.: Dimension-Six Terms in the Standard Model Lagrangian. JHEP **10**, 085 (2010). arXiv:1008.4884 [hep-ph]
55. Jenkins, E.E., Manohar, A.V., Stoffer, P.: Low-Energy Effective Field Theory below the Electroweak Scale: Operators and Matching. JHEP **03**, 016 (2018). arXiv:1709.04486 [hep-ph]
56. Brod, J., Gorbahn, M., Stamou, E.: Updated Standard Model Prediction for $K \to \pi\nu\bar{\nu}$ and ϵ_K. PoS BEAUTY2020, 056 (2021). arXiv:2105.02868 [hep-ph]
57. Feruglio, F., Paradisi, P., Pattori, A.: On the Importance of Electroweak Corrections for B Anomalies. JHEP **09**, 061 (2017). arXiv:1705.00929 [hep-ph]
58. Cornella, C., Feruglio, F., Paradisi, P.: Low-energy Effects of Lepton Flavour Universality Violation. JHEP **11**, 012 (2018). arXiv:1803.00945 [hep-ph]
59. Feruglio, F.: B-anomalies related to leptons and lepton flavour violation: new directions in model building. PoS BEAUTY2018, 029 (2018). arXiv:1808.01502 [hep-ph]
60. Aebischer, J., Kumar, J., Stangl, P., Straub, D.M.: A Global Likelihood for Precision Constraints and Flavour Anomalies. Eur. Phys. J. C **79**(6), 509 (2019). arXiv:1810.07698 [hep-ph]
61. Capdevila, B., Laa, U., Valencia, G.: Anatomy of a six-parameter fit to the $b \to s\ell^+\ell^-$ anomalies. Eur. Phys. J. C **79**(6), 462 (2019). arXiv:1811.10793 [hep-ph]
62. Crivellin, A., Greub, C., Müller, D., Saturnino, F.: Importance of Loop Effects in Explaining the Accumulated Evidence for New Physics in B Decays with a Vector Leptoquark. Phys. Rev. Lett. **122**(1), 011805 (2019). arXiv:1807.02068 [hep-ph]
63. LHCb Collaboration, Aaij, R., et al.: Measurement of lepton universality parameters in $B^+ \to K^+\ell^+\ell^-$ and $B^0 \to K^{*0}\ell^+\ell^-$ decays. Phys. Rev. D **108**(3), 032002 (2023). arXiv:2212.09153 [hep-ex]
64. BELLE Collaboration, Choudhury, S., et al.: Test of lepton flavor universality and search for lepton flavor violation in $B \to K\ell\ell$ decays. JHEP **03**, 105 (2021).arXiv:1908.01848 [hep-ex]
65. Chen, T., Guestrin, C.: XGBoost: A Scalable Tree Boosting System. arXiv:1603.02754 [cs.LG]
66. Fuentes-Martín, J., Isidori, G., König, M., Selimović, N.: Vector Leptoquarks Beyond Tree Level III: Vector-like Fermions and Flavor-Changing Transitions. Phys. Rev. D **102**, 115015 (2020). arXiv:2009.11296 [hep-ph]
67. Allwicher, L., Bordone, M., Isidori, G., Piazza, G., Stanzione, A.: Probing third-generation New Physics with $K \to \pi\nu\bar{\nu}$ and $B \to K^{(*)}\nu\bar{\nu}$. arXiv:2410.21444 [hep-ph]
68. Athron, P., Martinez, R., Sierra, C.: B meson anomalies and large $B^+ \to K^+\nu\overline{\nu}$ in non-universal U(1)$'$ models. JHEP **02**, 121 (2024). arXiv:2308.13426 [hep-ph]
69. Guedes, G., Olgoso, P.: From the EFT to the UV: the complete SMEFT one-loop dictionary. arXiv:2412.14253 [hep-ph]
70. Fuentes-Martín, J., Isidori, G., Pagès, J., Yamamoto, K.: With or without U(2)? Probing non-standard flavor and helicity structures in semileptonic B decays. Phys. Lett. B **800**, 135080 (2020). arXiv:1909.02519 [hep-ph]
71. Faroughy, D.A., Isidori, G., Wilsch, F., Yamamoto, K.: Flavour symmetries in the SMEFT. JHEP **08**, 166 (2020). arXiv:2005.05366 [hep-ph]